Supplementary Information: Spatially Resolved Thermoelectric Effects in operando Semiconductor-Metal Nanowire Heterostructures

Nadine Gächter,[1,*] Fabian Könemann,[1] Masiar Sistani,[2] Maximilian G. Bartmann,[2] Marilyne Sousa,[1] Philipp Staudinger,[1] Alois Lugstein,[2] and Bernd Gotsmann[1,†]

[1] *IBM Research - Zurich, 8803 Rüschlikon, Switzerland*
[2] *Institute of Solid State Electronics - TU Wien, 1040 Vienna, Austria*

(Dated: September 17, 2020)

I. DEVICE FABRICATION

The NWs are fabricated by thermally induced substitution of gold assisted vapor-liquid-solid (VLS) grown Ge-NWs by Al. At first, <111> oriented Ge-NWs are grown heteroepitaxially on silicon substrates in a low pressure chemical vapor deposition system by use of a gold-assisted VLS process. The NWs are then coated with 15 nm high-k Al_2O_3 by atomic layer deposition (ALD) and drop-cast on a highly p-doped Si substrate with a 100 nm thick dielectric layer of SiO_2. Afterwards, the Al-contacts are formed with electron-beam lithography, sputter deposition and lift-off techniques in preparation for the subsequent thermal exchange reaction. Lastly, in order to form the single crystalline Al-Ge-Al heterostructure, the Ge-NWs are thermally annealed at 623 K. Under these conditions, the diffusion constants of Ge and Al are 10^{12} times higher in Al than in Ge[1]. This means, that the Ge can easily diffuse into the Al-contact pats, whereas the Al-atoms are efficiently supplied via fast self-diffusion to take over the released lattice sites. The successive substitution of Ge-atoms with Al has been monitored *in-situ* in both, scanning electron microscopy (SEM) and scanning transmission electron microscopy (STEM) studies. They revealed atomically sharp interfaces between the Al and Ge during the anneal. Thus, the length L_{Ge} of the Ge-segment is tuned by varying the annealing time. For sufficiently long baking times the Ge diffuses completely out of the wire into the contact pads. It leaves behind single crystalline Al (c-Al) NWs with a single grain boundary in the center. Furthermore, the Ge-segments are integrated in a back-gated field effect transistor (FET) by construction. The Al-contacts are naturally self-aligned with the wire. More details are found in references [1–3].

* Correspondence email address: nadine.gaechter@unibas.ch
† Correspondence email address: bgo@zurich.ibm.com

II. NW PROPERTIES

Figure 1 b-d in the paper show a schematic, a STEM image of the cross-section and a SEM of the nanowire heterostructure studied here. More particularly it consists of a single-crystalline Ge-segment of 168 nm length and 37 nm diameter, as determined using scanning transmission electron microscopy (STEM). The Ge-segment is contacted by two self-aligned c-Al nanowires of the same diameter and around 1.7 μm length. An aluminium oxide shell (Al_2O_3) of 15 nm thickness deposited by atomic layer deposition (ALD) surrounds the Al-Ge-Al core. The interfaces between the c-Al and Ge are abrupt to the atomic level. The Al-sections of the nanowire are contacted using Al pads patterned with electron-beam lithography on a Si/SiO_2-substrate.

The electrical properties of pure c-Al nanowires fabricated using the same process revealed a conductivity of $\sigma = (7.6 \pm 1.5) \cdot 10^6\,(\Omega\mathrm{m})^{-1}$ for Al[3]. The Al-Ge-Al heterostructures with atomically abrupt interfaces show the non-linear current-voltage (IV) relationship of two back-to-back Schottky diodes in series for Ge-segments of length $L_{\mathrm{Ge}} > 45$ nm with an overall resistance proportional to the Ge-segment length[4]. From gating experiments it is further concluded that the Ge segments act like p-type semiconductors. Independent of metal type and doping concentrations, metal-germanium junctions form Schottky contacts, exhibiting very strong Fermi-level pinning close to the valence band [5, 6].

One issue regarding the thermal characterization of current-carrying Al-Ge-Al nanowires are traps for charge carriers located at the Ge/Ge-oxide interface. In this regard, the protective Al_2O_3-shell ensures reliable and reproducible measurements by avoiding any influence of adsorbates rather than eliminating charge trapping due to dangling bonds at the Ge/Ge-oxide interface. These traps lead to hysteretic current voltage relationships. However, the hysteresis decreases with increasing current range, drive speed and operating time. It was found that for currents larger than 21 μA, the hysteresis is reduced and the current-voltage graph sufficiently linear to assume a constant resistance in the thermal analysis. Consequently, we estimate a contri-

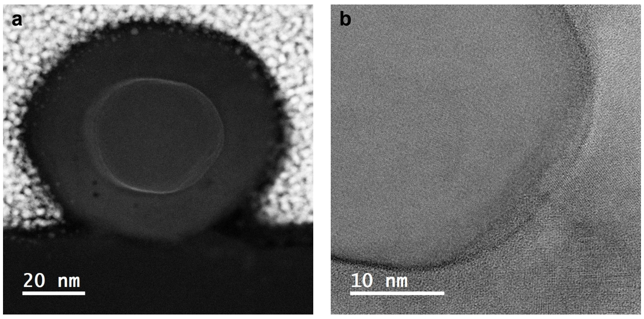

Figure 1. DF-STEM scans taken after the thermal measurements. The oxide Aluminium Oxide layer shows a certain degree of crystalinity which enhances the thermal conductivity.

bution to the systematic error to the extracted temperature values for lower currents shown below due to these charging effects.

III. IMAGING AND GEOMETRIC CHARACTERIZATION OF THE WIRE

After the thermal scans, a scanning transmission electron microscopy analysis of an Al segment is carried out with a double spherical aberration-corrected JEOL JEM- ARM200F operated at 200 kV. The Al segment was prepared by focused ion beam, using a dual beam FIB Helios NanoLab 660 from FEI. The DF STEM images of the cross-section are shown in figure 1 and reflect the round shape. A sharp interface separates the core and the oxide shell with respective areas of $A_{\mathrm{core}} = 1075{\pm}80\,\mathrm{nm}^2$ and $A_{\mathrm{shell}} = 2450{\pm}230\,\mathrm{nm}^2$. The Al-core shows some poly-crystallinity, however, the loss of crystalline order probably occurred during sample preparation in the FIB. Previous more extensive studies suggest crystalline order. Furthermore, the Al_2O_3-shell is observed to be crystalline in the Fourier image of the cross-section (not shown here).

Energy Dispersive X-ray Spectroscopy (EDS) chemical maps reveal a well defined Al-core and Al_2O_3 shell with a sharp transition between the two. No residual Ge is detected beyond the detection limit which does not resolve doping concentrations. They are shown in figure 2. To conclude, all geometric properties of the NW are measured and summarized in table I.

Finally, figure 3 shows the SEM-image taken in the FIB, when the wire was no longer conducting. The location at which the wire broke, lies close to the upper Al-electrode. In most of the experiments the wires break in a similar spot, even though the heating is observed closer to the Ge-segment. The wire is slightly thinner towards the electrodes due to the chemical etching of the oxide shell before the deposition of the electrodes.

L_{wire}	$(2475 \pm 5)\,\mathrm{nm}$
L_{Ge}	$(168 \pm 1)\,\mathrm{nm}$
r_{core}	$(18.5 \pm 2)\,\mathrm{nm}$
d_{oxide}	$(15 \pm 2)\,\mathrm{nm}$
d_{touch}	$(56 \pm 5)\,\mathrm{nm}$
A_{core}	$(1075 \pm 80)\,\mathrm{nm}^2$
A_{shell}	$(2450 \pm 230\,\mathrm{nm}^2$
A_{wire}	$(0.0035 \pm 0.0003)\,\mu\mathrm{m}^2$

Table I. Geometric properties of the NW obtained from SEM and STEM images: L_{Ge} is the length of the Ge segment, r_{core} is the radius of the conducting core, d_{oxide} is the thickness of the surrounding Al_2O_3 shell, d_{touch} is the length perpendicular to the wire that is in contact with the substrate. A_{core}, A_{shell} and A_{wire} are the cross-sections of the conducting inner core, the passivating Al_2O_3 shell and the entire wire respectively. The error estimation for the areas follows Gaussian error propagation.

IV. ELECTRICAL CHARACTERIZATION OF THE NANOWIRE

This section provides some overview on the electrical behavior of the NW under measuring conditions for the thermal scans. Figure 4 displays the I-V relation that is taken just below the threshold voltage at which any heating of the wire is detected. The I-V has two very striking features: First, a pronounced hysteresis appears between ramping the current up and down. Second, the electrical resistance depends highly on the applied voltage. Both observations are well visible on the resistance-voltage (R-V) plot in the logarithmic scale depicted next to the I-V. It reveals a change in resistance of two orders of magnitude. A heating of the wire is observed only if the applied electric field is higher than the electrical breakdown field in pure Ge wires that has been previously observed at $E = 1.25 \cdot 10^5\,\mathrm{V/cm}$ [7]. For a Ge-segment of length $L_{\mathrm{Ge}} = 168\,\mathrm{nm}$ this corresponds to an applied voltage bias of $V_{\mathrm{bias}} = 2.1\,\mathrm{V}$.

The wire is integrated in an electrical circuit including a series resistor of similar resistance $R_{\mathrm{S}} = 100\,\mathrm{k\Omega}$ that protects from current spikes. The real time data acquisition system is is also used to measure the IV after each scan. The IV is conducted in the DC-mode with 200 steps distributed over the AC-modulation. Each point is averaged over 20 ms.

Figure 4 shows a plot of all I-V and R-V curves going up to the maximum voltage bias applied in the respective thermal measurements. The electric field in the Ge-segment is between $E \approx V_{\mathrm{device}}/L_{\mathrm{Ge}} = 1.27 - 1.44 \cdot 10^5\,\mathrm{V/cm}$. Each curves is recorded after one hour of operation time and, therefore, charging of the oxide shell during the thermal scan. The wires have some seconds to cool down after the scan. The very

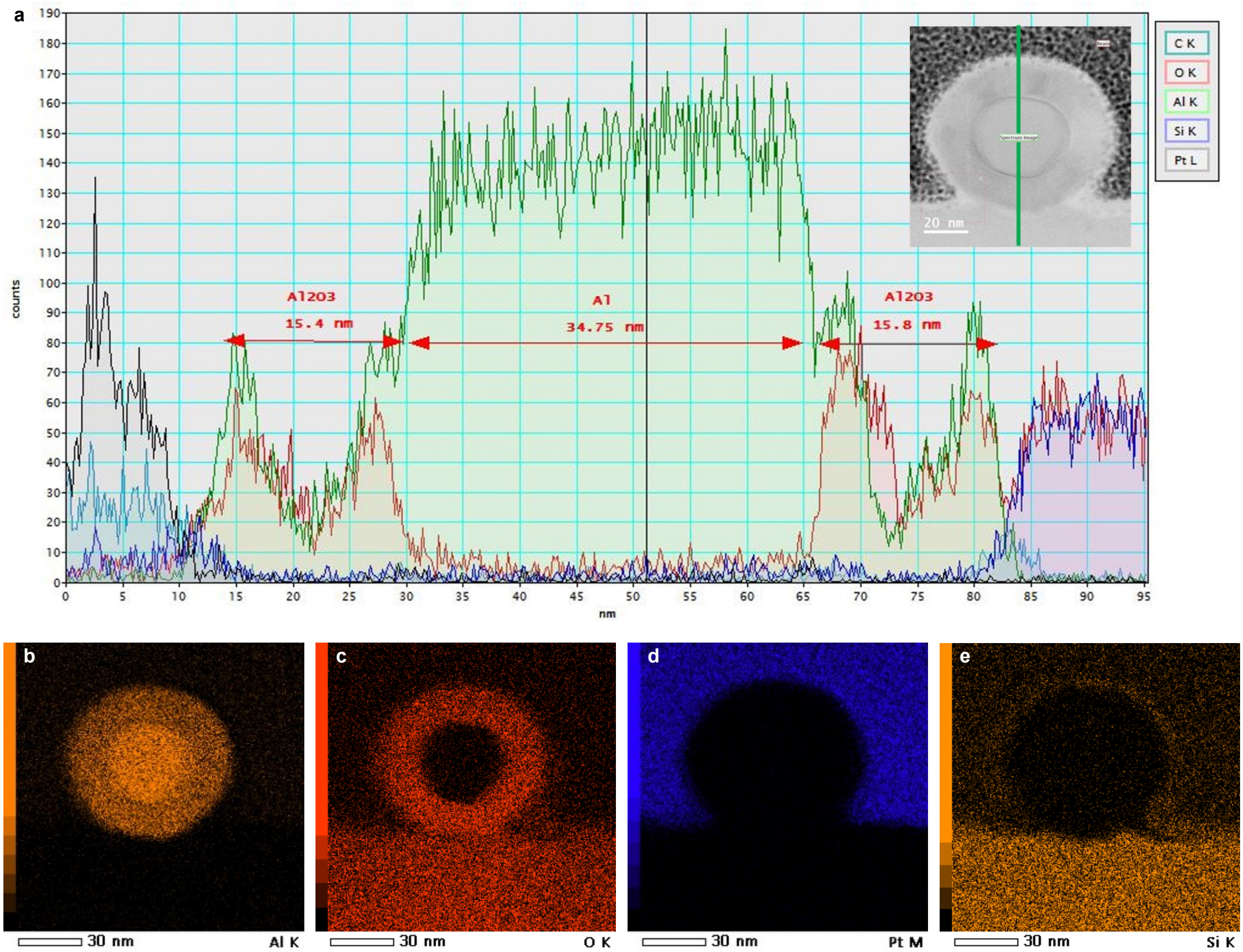

Figure 2. Chemical Analysis (EDS) of the nanowire cross-section. a) Along the a line through the center of the wire's cross-section, see the green line on the STEM image in the inset. b), c), d), e) show the number of counts at the energy of the Al, O, Pt and Si respectively. They demonstrate the high purity of the different materials. The platinum was deposited after the thermal measurements, to protect the wire before the FIB cut.

different behavior of the IVs for different maximally applied voltages is, therefore, not caused by changes in the device temperature which should be the same for equal current density. Hence, it might be attributed to the charging effect in the oxide shell. Moreover, the amount of charging depends upon whether the NW is operated under AC- or DC-current. It is observed, that this local gating phenomenon changes the resistance of the device by orders of magnitude for only small changes of the experimental condition. However, the amount of charging tends to a stationary state when the IV is run quickly several times. Therefore, the hysteresis is expected to disappear sufficiently during the scans in the SThM. A difficulty for investigating thermoelectric effects is the simultaneous presence of Joule heating, which, on the other hand, creates a positive feedback phenomenon by decreasing the resistance during heating. It is counteracted only by an increased charge carrier scattering at higher temperature.

An increase in drain current with the gate voltage is linked to the trapping of negative surface charges in the interband levels due to surface states and bulk impurities. An applied negative gate voltage provokes the accumulation of holes that continuously neutralize the trapped electrons[4]. A similar p-type charging has been shown to appear in undoped Si-NWs. In the Si-system, changing the passivation layer from Al-oxide to Si-oxide turns the device into a n-type FET, being OFF for negative gate voltage. Therefore, surface charges originating from interface defects and dangling bonds can generate doping effects in NWs[8]. The use of a high quality thermal oxide reduces the number of charge traps and thereby also the hysteresis that occurs when the gate voltage is sweeped from negative to positive

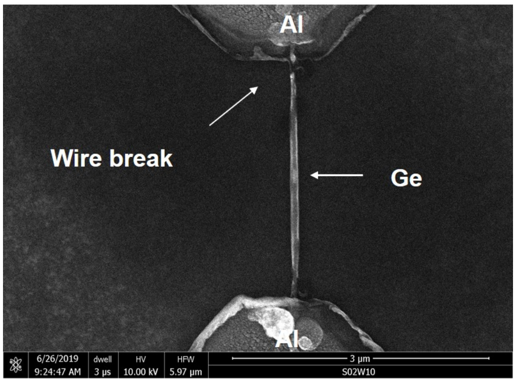

Figure 3. The SEM image after the thermal scans when the wire was no longer conducting. The breaking point lies close to the electrodes, even though the thermal scans revealed only little heating in these areas.

values and vice versa[4]. Under a given gate voltage, the neutralization of holes is a rather slow process. It reaches a stationary state after approximately 20 minutes of operation. Such a long time-span is owed to a kinetic limitation by either a diffusion or tunnel barrier in form of a GeO_x layer at the interface between the Ge and the Al_2O_3. Indeed, such a layer is expected to form during ALD-deposition of the Al_2O_3 layer. It acts as a local gate and provides a large number of trapping states[9][10]. To conclude, the nature of the passivation layer highly influences the reliability and reproducible performance of the device under the above described charging mechanism.

The electrical resistivity in the Ge-segment is determined as follows. It is calculated from the electrical resistance measured in the I-V curves which are taken after each scan. The resistance at the maximal voltage in the I-V is the same as the AC-voltage applied during the scan closest to the conditions during the respective thermal measurement. The contribution of the Al-wire and contacts is subtracted from the overall device resistance. The values are represented as a function of the average temperature in the Ge-segment in figure 5. The electrical resistivity depends strongly on the temperature.

V. STHM OPERATION AND ANALYSIS DETAILS

The images of the scans are generated and treated with the help of the open-source software Gwyddion. Apart from the straight forward calculation of the temperature field using equation 1 in the paper, some further data processing is conducted: Firstly, under the observation that the trace and retrace are nearly identical, they are averaged for noise reduction. Secondly, a low-pass scaling is applied to compensate for the signal attenuation that is due to a delay in temperature response of the cantilever. Thirdly, a DC-signal offset is manually corrected to eliminate some remaining non-uniformity in the temperature field which is caused by the artifacts in the DC-field. It is hard to measure the temperature offset of the sensor exactly due to small changes in DC-signal when approaching the tip. However, by eye it is easy to see when the artifacts at the edge of the NW disappear. The procedure might be compared to aligning a microscope. The final heat maps are shown in figure 2.

When turning the focus to the temperature profile around the Al-Ge interface, the location of the Ge segment on the temperature line has to be determined first. The temperature gradient of the Joule profile is plotted in figure 6a). A pronounced maximum and minimum peak marks the deflection points in the Joule profile. They result from a sudden change of the thermal and electrical conductivities between the Ge- and the Al-parts. Their distance of 169 nm corresponds precisely to the expected length of the Ge-segment in a scan with 10 nm resolution. The hereby identified location of the Ge-segment is then shaded in red on the profile lines and used as orientation in the following analysis. After the deflection point there is a transition length of about 40-50 nm, that is well seen on the zoom-in figure 6b). This area corresponds to the phonon-electron thermalization that is blurred by a combination of the spatial resolution and a parallel heat transport in the oxide shell.

In general, the temperature profiles show mostly symmetric behavior for the Joule and the Peltier signal. It reflects the good quality of the measurement data and the sample. However for the thermal measurements that were conducted at lower operating currents, the profile curves show a slight asymmetry. This is when the SThM method reaches its limitations due to the underlying assumption of a linear electrical behavior of the sample. This requirement is better fulfilled at higher currents and leads to a mixing of the $1f_{\mathrm{mod}}$ and $2f_{\mathrm{mod}}$ signal at lower currents. Nonetheless, the comparison of the the maximum temperature in the Joule-scan with the dissipated power and the comparison between the maximum temperature difference in the Peltier-scan and the current reveal linear relationships. These results is expected under the the 1D diffusion equation 2 from the paper. They can be seen in figure 7. The noise levels are quite low. No noise reduction is used at any stage in the lateral direction of the wire, to omit altering the shape of the profile. The expected error on the measured temperature is a combination of a constant absolute error and a more important relative contribution that depends on the sample temperature. The absolute error is determined by taking the root mean squared of the temperature on the substrate far

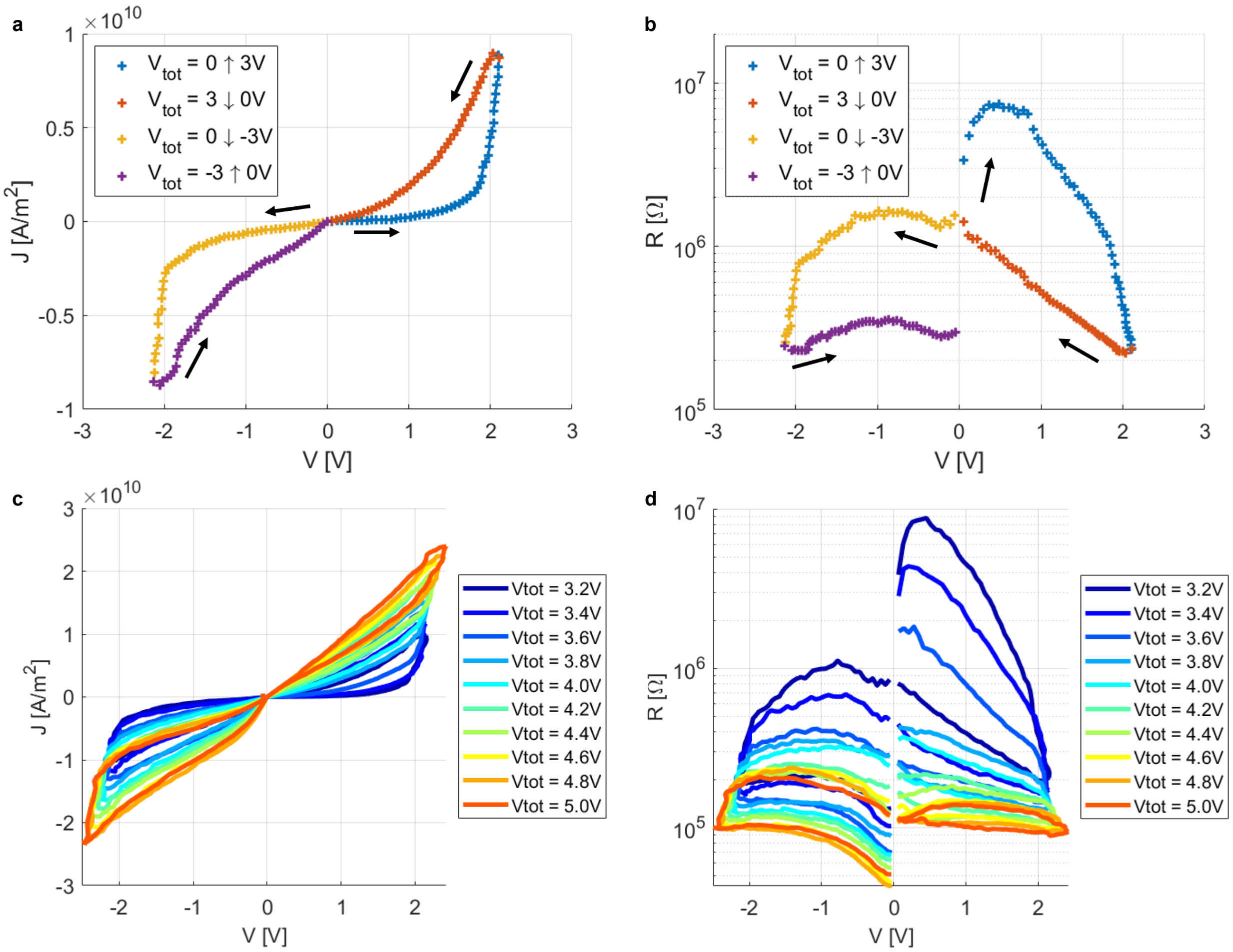

Figure 4. Characterization of the electrical behavior of the nanowire. The data in a) and b) is measured just below a current density J is that is high enough to lead to a detectable change in the temperature for the wire. a) is the current density is represented as a function of the voltage drop over the device, b) the same information shown with the device resistance as a function of the voltage drop over the NW. c) and d) show the I-V and R-V curves measured immediately after each SthM scan up to the same voltage bias. The total applied voltage v_{tot} drops additionally over a series resistance of $R_{\mathrm{S}} = 100\,\mathrm{k\Omega}$.

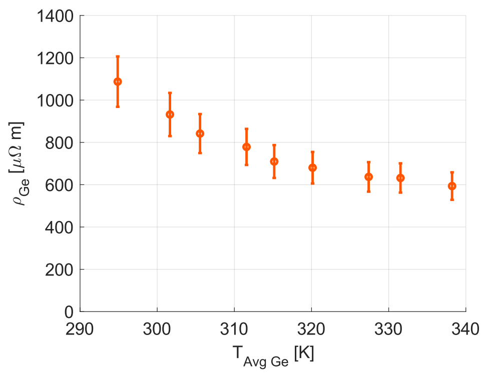

Figure 5. The electrical resistivity ρ_{Ge} is shown as a function of the average temperature in the Ge segment.

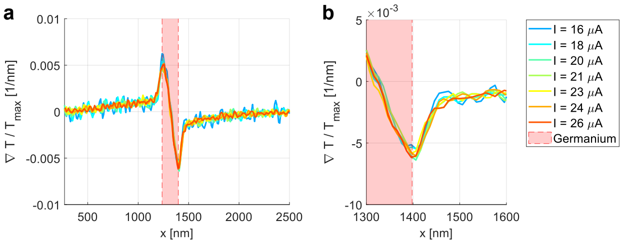

Figure 6. Determination of the location of the Ge segment is possible due to a discontinuity in the temperature gradient at the thermal interface between the Ge and the Al segments. a) The temperature gradient $\nabla T_{\mathrm{Joule}}$ as a function of the position x along the wire for the different operating currents. The gradients are normalized by the maximum temperature in the center of the red shaded Ge segment. b) shows a zoom on the gradient at the Ge-Al interface.

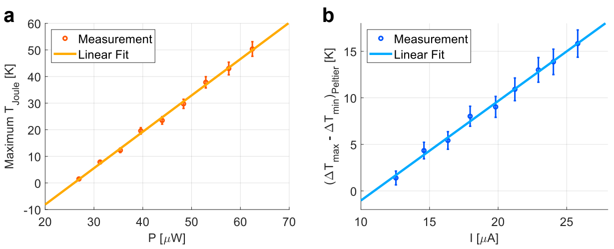

Figure 7. In a), the maximum temperature increase caused by Joule heating is plotted as a function of the dissipated power P. In b), the temperature difference between the two poles in the Peltier scan as a function of the operating current. The errorbars reflect the uncertainties on the temperature measurement.

from the wire where no signal is expected. The relative error the result of a multiplication with the temperature difference to the sensor according to equation 1 is estimated to be around 5% of the sample temperature[11]. The estimated uncertainty for each temperature measurement along the profile of the NW is then calculated as

$$\Delta\left(\Delta T_{\mathrm{J/P}}\right) = \frac{1.84[\mathrm{K}]}{\sqrt{15}} + 0.05 \cdot \Delta T_{\mathrm{J/P}} \tag{1}$$

The radiated thermal heat per unit length at the maximum temperature of $T_{max} = 323\,\mathrm{K}$ is calculated as $P_{rad} = 2 \cdot \pi \cdot r \cdot \sigma \cdot T^4 \approx 1.29 \cdot 10^{-4}\,\mathrm{W/m}$ compared to a heat loss to the substrate per unit length of $P_{subst} = g \cdot T \approx 642\,\mathrm{W/m}$. In these equations, r is the wire radius and σ the Boltzmann constant. Therefore, the term attributed to thermal radiation is neglected. To conclude, the method allows to resolve the temperature profiles of the samples that are caused by the Joule and Peltier effects down to the thermalization lengths of the heat carriers. In order to extract further information by the most simple means, the analysis is divided in

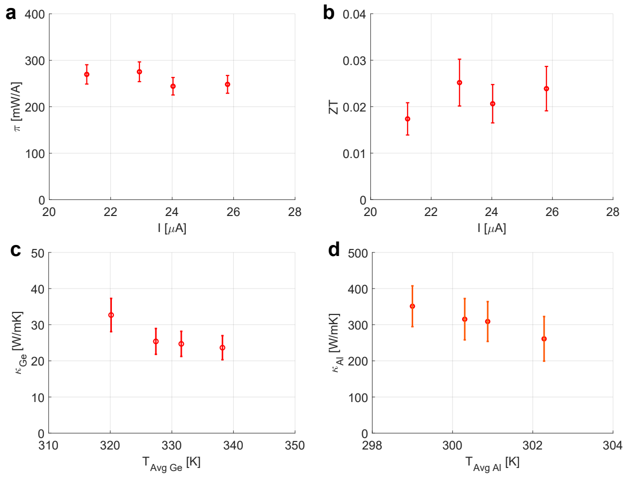

Figure 8. In a) the Peltier coefficient and in b) the ZT value as a function of the operating current. In c) and d) the thermal conductivities of the Ge and the Al segment of the wire as a function of the segment's average temperature. In this representation, the parallel conduction in the oxide shell of the Al segment is not accounted for, which leads to a slight overestimation of the values.

different sectors on the wire. For completeness, the extracted values of the Peltier coefficient and the ZT value as a function of the operating current are provided in figure 8. Also, the extracted thermal conductivities of the respective wire segment is shown in (c) and (d) as a function of the segment's average temperature.

VI. JOULE HEATING IN PURE ALUMINIUM NANOWIRES

Thermal measurements are also conducted on a c-Al NW. However, the electrical characterization indicates leaking of the device. Nonetheless, the thermal measurements give some insight on where heat is generated. The Joule heat map in figure 9 shows heating of the entire wire, compared to the Al-Ge-wire, where it is more localized around the Ge-segment. Even more striking is the heating of the contacts which is not present in the heterostructure. In the profile lines along the wire, also shown in figure A.4, a distinct heat source is identified. Most probably it is located where the Ge-segment disappeared during fabrication, leaving behind some grain boundary or impurities inducing more scattering of electrons during operation. Consequently, the electrical conductivity of the single crystalline Al-parts of the heterostructure wire is expected to be higher than the values determined for the entire c-Al-wires due to the absence of this defect.

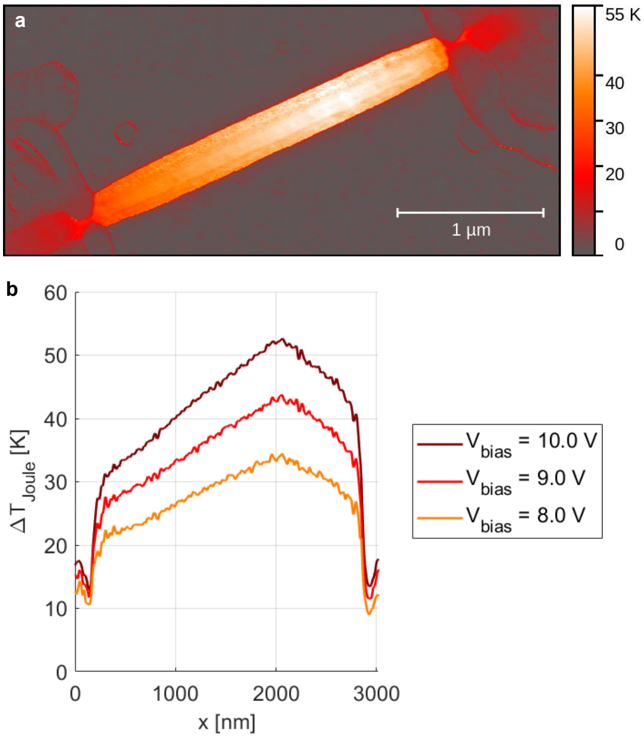

Figure 9. Joule heating in an operando c-Al wire. a) shows the heat map measured with the SThM and b) shows the temperature profile along the nanowire axis under different voltage bias.

[1] K. El hajraoui, M. A. Luong, E. Robin, F. Brunbauer, C. Zeiner, A. Lugstein, P. Gentile, J.-L. Rouvière, and M. Den Hertog, Nano Letters **19**, 2897 (2019).

[2] S. Kral, C. Zeiner, M. Stöger-Pollach, E. Bertagnolli, M. I. den Hertog, M. Lopez-Haro, E. Robin, K. El Hajraoui, and A. Lugstein, Nano Letters **15**, 4783 (2015).

[3] F. M. Brunbauer, E. Bertagnolli, J. Majer, and A. Lugstein, Nanotechnology **27**, 385704 (2016).

[4] M. Sistani, P. Staudinger, J. Greil, M. Holzbauer, H. Detz, E. Bertagnolli, and A. Lugstein, Nano Letters **17**, 4556 (2017).

[5] A. Thanailakis and D. C. Northrop, Solid-State Electronics **16**, 1383 (1973).

[6] A. Dimoulas, P. Tsipas, A. Sotiropoulos, and E. K. Evangelou, Applied Physics Letters **89**, 252110 (2006).

[7] A. Lugstein, M. Mijić, T. Burchhart, C. Zeiner, R. Langegger, M. Schneider, U. Schmid, and E. Bertagnolli, Nanotechnology **24**, 65701 (2013).

[8] K. Winkler, E. Bertagnolli, and A. Lugstein, Nano Letters **15**, 1780 (2015).

[9] L. Zhang, H. Li, Y. Guo, K. Tang, J. Woicik, J. Robertson, and P. C. McIntyre, ACS Applied Materials & Interfaces **7**, 20499 (2015).

[10] P. Staudinger, M. Sistani, J. Greil, E. Bertagnolli, and A. Lugstein, Nano Letters **18**, 5030 (2018).

[11] F. Könemann, M. Vollmann, T. Wagner, N. Mohd Ghazali, T. Yamaguchi, A. Stemmer, K. Ishibashi, and B. Gotsmann, The Journal of Physical Chemistry C **123**, 12460 (2019).